Materials Science and Engineering A 538 (2012) 58–62

Contents lists available at SciVerse ScienceDirect

Materials Science and Engineering A

journal homepage: www.elsevier.com/locate/msea

Determining effective radius and frame compliance in spherical nanoindentation

Seung-Kyun Kang[a], Young-Cheon Kim[a], Yun-Hee Lee[b], Ju-Young Kim[c,*], Dongil Kwon[a]

[a] Department of Materials Science and Engineering, Seoul National University, Seoul 151-744, South Korea
[b] Division of Industrial Metrology, Korea Research Institute of Standards and Science (KRISS), Daejeon 305-340, South Korea
[c] School of Mechanical & Advanced Materials Engineering, UNIST, Ulsan 689-798, South Korea

ARTICLE INFO

Article history:
Received 8 November 2011
Received in revised form 5 January 2012
Accepted 6 January 2012
Available online 16 January 2012

Keywords:
Nanoindentation
Spherical indenter
Frame compliance
Tip bluntness
Elastic modulus

ABSTRACT

We estimate effective radii of a spherical nanoindenter at various indentation depths using Hertz elastic contact theory for the fully elastic contact region and AFM profiling residual indentation marks for the elastoplastic contact region. Using frame compliance measured as a function of indentation depth and the concept of infinitesimal deformation of a spherical nanoindenter, we introduce a profile of indentation–depth-dependent frame compliance that successfully explains the variation in frame compliance over the entire contact region. After using this indentation–depth-dependent frame compliance, we evaluated more consistent indenter radii from Hertz elastic contact theory at shallow indentation depths (<90 nm).

1. Introduction

Nanoindentation has been widely used to evaluate the mechanical response of materials at small scales. The advantage of nanoindentation is that the contact area is determined without needing to observe residual indentation marks. Two factors that should be taken into account in determining contact area are corrections for imperfect indenter geometry and frame compliance. Oliver and Pharr introduced corrections for imperfect indenter geometry by using area functions and frame compliance corrections in a series of nanoindentations on a standard sample with known elastic modulus and Poisson's ratio [1–5]; these methods have been in general use to date. In these methods, the following equation is used to derive frame compliance:

$$\frac{1}{S_{\text{total}}} = C_{\text{frame}} + \frac{1}{S_{\text{sample}}} = C_{\text{frame}} + \frac{\sqrt{\pi}}{2E_r\sqrt{A_c}}, \quad (1)$$

where S_{total} is the initial unloading stiffness from the indentation force–depth curve, C_{frame} is frame compliance, S_{sample} is sample stiffness, E_r is reduced elastic modulus, and A_c is contact area. C_{frame} is determined from the intercept of $1/S_{\text{total}}$ and $1/\sqrt{A_c}$ curve on the condition of constant C_{frame} and E_r regardless of indentation depth [1]. The methodologies are also valid for spherical indenters as well as sharp indenters such as the Berkovich indenter. By using the definition of hardness ($H = P_{\max}/A_c$), Eq. (1) is rewritten as

$$\frac{1}{S_{\text{total}}} = C_{\text{frame}} + \frac{\sqrt{\pi}\sqrt{H}}{2E_r\sqrt{P_{\max}}}, \quad (2)$$

where $P_{\max}$ is the maximum indentation force. The frame compliance is determined from the intercept of $1/S_{\text{total}}$ and $1/\sqrt{P_{\max}}$ curve on the condition of constant C_{frame}, E_r, and H regardless of indentation depth. This method is valid only for sharp indenters, which evaluate constant hardness independent of indentation depth, because it has a geometrical self-similarity (note that this method is also valid only with no indentation size effect).

The sharp indenter obtains invariant hardness with a single indenter by varying indentation depth. So the sharp indenter, especially the Berkovich indenter, is widely used to evaluate hardness and elastic modulus in nanoindentation. Unlike sharp indenters, the spherical indenter is not geometrically self-similar, and this makes it possible to derive the various stress–strain fields underneath it by varying indentation depths. This enviable feature of the spherical indenter, along with progress in manufacturing spherical indenters at small scales, is accelerating its applications in nanoindentation as well as at micro- and macro-scales [6–10]. Research on calibrating the indenter imperfection of spherical indenter on macro- to nanoscale [4,11–14] and the variation of

* Corresponding author. Tel.: +82 52 217 2334; fax: +82 52 217 2309.
E-mail address: juyoung@unist.ac.kr (J.-Y. Kim).

0921-5093/$ – see front matter © 2012 Elsevier B.V. All rights reserved.
doi:10.1016/j.msea.2012.01.013

frame compliance in spherical indenter has been performed at the macroscale [4,5]. However, the frame compliance for spherical indenter remains unexplored at nanoscale. Because calibrating indenter geometry and frame compliance mutually affect each other, systematic investigation of both the variation of frame compliance and indenter imperfection is required for spherical indentation at nanoscale.

The radius of a spherical indenter can be measured on the force–depth curve in the fully elastic regime by using the Hertz equation, given by

$$P = \frac{4}{3}E_r\sqrt{R}h^{3/2} \tag{3}$$

where P is the indentation force, R is the indenter radius, and h is the indentation depth [14,15]. This method is valid only in the fully elastic regime. In the elastoplastic deformation regime, a residual impression corresponding to plastic deformation remains after unloading. Profiling this residual impression makes it possible to measure the radius of spherical indenter using the simple geometrical relation

$$R = \frac{(A_c/\pi) + h_c^2}{2h_c}, \tag{4}$$

where h_c is the contact depth of the residual indentation mark [4].

Here we discuss the issues of indenter geometry and frame compliance in spherical nanoindentation, and suggest novel methodologies to correct these factors quantitatively. We compare indenter radii measured by two methodologies: fitting the Hertz equation to the force–depth curve in the fully elastic regime, and profiling the residual impression in the elastoplastic regime. We also investigate frame compliance due to deformation of the spherical indenter, which was found to vary with indentation depth. It is also shown that the variation in frame compliance affects the determination of indenter geometry when one uses the Hertz equation-fitting method. Finally, we propose calibrations of the functional frame compliance to determine coherent indenter radii in the two methodologies.

2. Experiments

We prepared a diamond spherical indenter (Micro Star Technologies Inc., TX, USA) made by blunting a conical indenter. The nominal indenter radius, 5 μm, was estimated by analyzing the side-view TEM image of the indenter. We conducted a series of nanoindentations with the spherical indenter on the fused silica with elastic modulus 72 GPa and Poisson's ratio 0.17 at maximum indentation depth of 90 nm using the Nanoindenter XP (Agilent, USA). We confirmed that loading and unloading curves are identical up to an indentation depth of 90 nm, and that the curves are irreversible by plastic deformation at indentation depths greater than 90 nm. To measure the indenter radius at indentation depths greater than 90 nm, we profiled residual indentation marks in 3D using atomic force microscopy (AFM), the SIS NanostationII AFM. To verify frame compliance, we prepared four metal samples, Al, Cu, Ni, and SCM4, of elastic moduli 70, 125, 200 and 210 GPa, respectively, as measured by an ultrasonic pulse-echo technique using a two-channel digital real-time oscilloscope. The surfaces were electropolished after mechanical polishing with 0.05 μm diamond powder. We evaluated the constant frame compliance using Eq. (2) by performing a series of nanoindentation on fused silica with indentation depth from 1500 nm to 1800 nm with a Berkovich indenter, whose holder was the same as the spherical indenter.

3. Results and discussion

Fig. 1a shows the effective radius as measured from the Hertz equation for indentation depth less than 90 nm (red dotted lines), and from direct AFM profiling of the residual indentation marks for indentation depths greater than 90 nm (solid dots). Fig. 1b shows the indentation force–depth curve with maximum indentation depth of 90 nm. Fitting Eq. (3) to the force–depth curve as shown in Fig. 1a suggests that the effective indenter radius for indentation depths between 0 and 90 nm is 3.36 ± 0.09 μm, which is substantially smaller than the nominal radius of 5 μm. It is important to note that in obtaining the indentation force–depth curve, we used a constant frame compliance 123.46 nm/N determined with the Berkovich indenter in the same apparatus by the Oliver–Pharr method. Fig. 1c shows a typical profile of residual impression with maximum indentation depth of 690 nm. The effective radius can be directly measured from the profiling by using Eq. (4). The measured effective radius of the spherical nanoindenter is 4.84 ± 0.20 μm (from 4.66 to 5.10 μm) for indentation depths between 250 and 700 nm, which is closer to the nominal value of 5 μm than that determined at shallow indentation depths by the Hertz equation.

At greater indentation depths, the effective radius measured by the Hertz equation for shallow indentation depths are quite different from that found by direct AFM profiling. We suspected that this difference could be due to incorrect frame compliance, since we used a constant frame compliance determined with the Berkovich indenter in the apparatus described above. While frame compliance does not affect the effective radius measured by 3D profiling of the residual impression because it does not use the indentation force–depth curve but instead directly profiles the residual impression, an incorrect correction for frame compliance directly affects the evaluated effective indenter radius evaluated from the Hertz equation since it utilizes indentation force–depth data.

To verify this presumption quantitatively, nanoindentation tests were performed with the spherical indenter on the Al, Cu, Ni, and SCM4 at seven different indentation depths from 50 to 1500 nm. Elastic moduli were calculated by the following relations:

$$E_r = \frac{\sqrt{\pi}}{2\sqrt{A_c}}S_{\text{sample}}, \tag{5}$$

$$\frac{1}{E_r} = \frac{(1-\nu^2)}{E} + \frac{(1-\nu_t^2)}{E_t} \tag{6}$$

where E and ν are the elastic modulus and Poisson's ratio of the sample, and E_t and ν_t are the elastic modulus and Poisson's ratio of the indenter [1–6,16,17]. Fig. 2a shows the elastic modulus as a function of indentation depth as measured by nanoindentation at each depth. Note that when calculating contact areas, we used the Oliver–Pharr method with nominal effective radius 4.84 μm for relative comparison of elastic moduli at various indentation depths. Though the effective radius was 3.3 μm evaluated by the Hertz method below 90 nm indentation depth, we also used a radius of 4.84 μm for those shallow indentation depths due to concerns about frame compliance. Even when using this directly measured effective indenter radius instead of a constant nominal radius, the elastic modulus increases gradually with increasing indentation depth in these four materials. This observation is consistent with previous spherical nanoindentation and macro-indentation testing using a sharp indenter [4,18].

By rewriting Eq. (1), frame compliance can be expressed as

$$C_{\text{frame}} = \frac{1}{S_{\text{total}}} - \frac{\sqrt{\pi}}{2E_r\sqrt{A_c}}. \tag{7}$$

We calculated frame compliances from Eq. (7) by using elastic moduli measured with ultrasonic pulse-echo techniques and

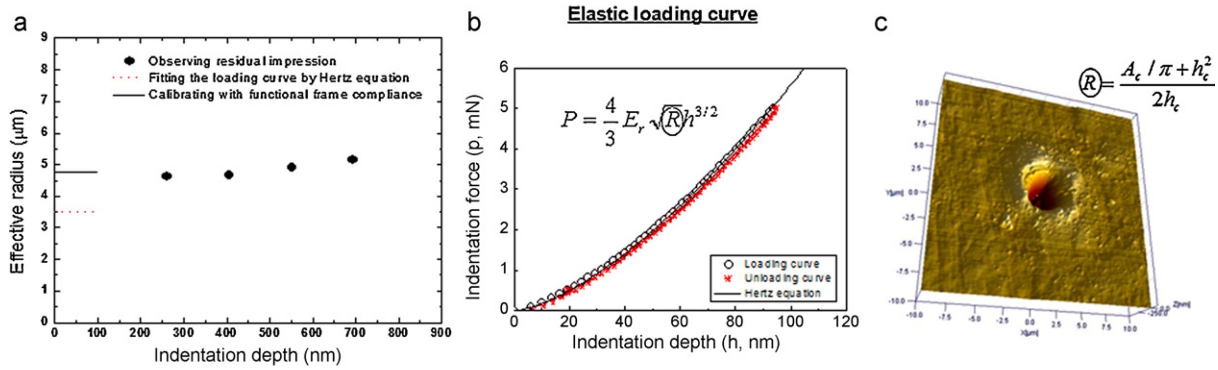

Fig. 1. (a) Effective radii of spherical indenter at each indentation depth evaluated by the two different methods; (b) fitting the Hertz equation to force–depth data for indentation depths less than 90 nm and (c) AFM profiling of the residual impression for indentation depths greater than 90 nm. (For interpretation of the references to color in this text, the reader is referred to the web version of this article.)

stiffness and contact area from the indentation force–depth curve. Fig. 2b shows the equivalent frame compliance, which is additionally required frame compliance for the actual sample elastic moduli using Eq. (7) for the four samples at various indentation depths. Because the modulus and compliance are inversely proportional, as shown in Eq. (7), and the measured elastic modulus increases gradually with increasing indentation depth, the equivalent frame compliance in Fig. 2b decreases with increasing indentation depth.

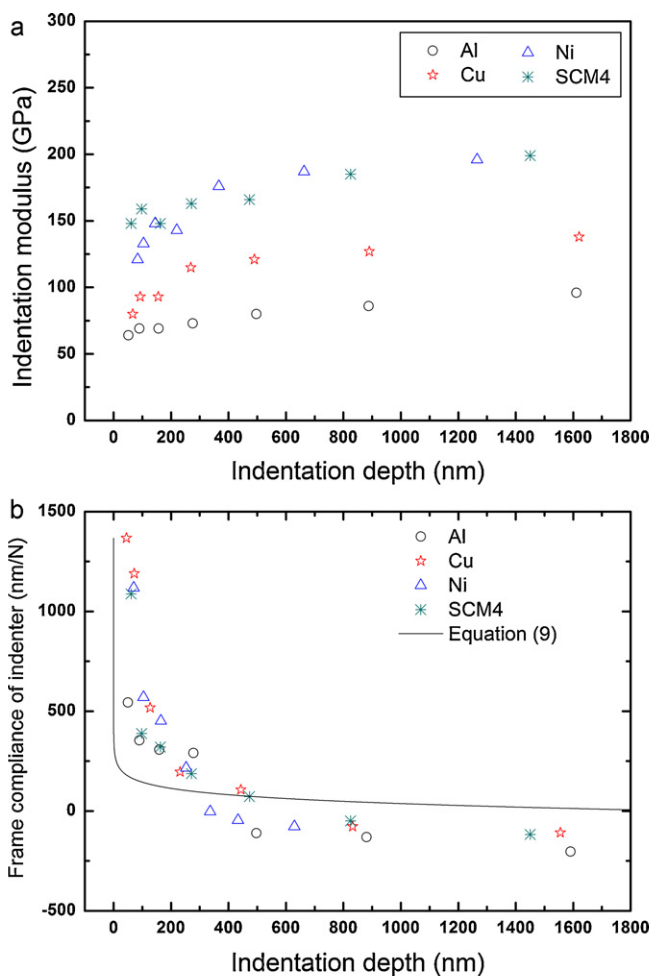

Fig. 2. (a) Elastic moduli of four metals, Al, Cu, Ni, and SCM4, analyzed using constant frame compliance, and (b) frame compliances of indenter derived from true elastic moduli and infinitesimal cylindrical frame model.

To understand the deviation of frame compliance, we introduce in Fig. 3 the concept of infinitesimal deformation of the indenter itself. In this framework, the boundary between the indenter and the frame is the contact area; i.e. only the indenter below the contact area is the effective indenter, and the remaining indenter and machine frame above the contact area are the effective frame. Frame compliance is expressed by summation of frame compliance of remaining indenter (C_{indenter}) and machine frame (C_0) as

$$C_{\text{frame}} = C_{\text{indenter}} + C_0. \tag{8}$$

The boundary of machine frame part is independent of indentation depth, so C_0 is constant. As indentation depth increases, on the other hand, C_{indenter} decreases because the frame boundary as well as the contact boundary increases with increasing indentation depth. In previous spherical macro-indentation work [4], we describe the spherical indenter as a summation of infinitesimal cylindrical frame as shown in Fig. 3, and the frame compliance can be derived from the following relation:

$$\begin{aligned} C_{\text{indenter}} &= \frac{1}{E_t}\cdot\frac{l-h}{\pi}\lim_{n\to\infty}\sum_{k=1}^{n}\frac{1}{2R\left(h+\frac{(k-1)(l-h)}{n}\right)-\left(h+\frac{(k-1)(l-h)}{n}\right)^2}\cdot\frac{1}{n} \\ &= \frac{1}{E_t}\cdot\frac{1}{\pi}\cdot\frac{1}{2R}\cdot\ln\frac{l}{(2R-l)}\left(\frac{2R}{h}-1\right) \end{aligned} \tag{9}$$

where l is the total height of the spherical indenter and k is the number of parts [4]. This equation relies only on the geometry and elastic modulus of the indenter, and thus is not expected to depend on the response of the sample.

Fig. 2b shows the expected frame compliance of indenter from Eq. (9), with $R = 4.84\,\mu\text{m}$, $l = 500\,\text{nm}$, and $E_t = 1050\,\text{GPa}$ from the geometry and elastic modulus of the indenter. Average values of effective indenter radius from 250 to 700 nm were used. The expected frame compliance of indenter in Fig. 2b shows a trend similar to the experimental data, implying that frame compliance should not be taken as constant but should be calibrated as a function of indentation depth, especially for spherical nanoindentation. Here we found negative frame compliance of the indenter above 500 nm indentation depth. This unexpected result is believed to arise from the estimation of frame compliance at the machine frame C_0. In the experimental evaluation of C_{indenter}, we used C_0 derived from a Berkovich indenter as a constant frame compliance. As the indentation depth is close to the indenter length during evaluation of C_0, C_0 is believed to be close to the machine frame compliance by neglecting frame compliance of the Berkovich indenter [1]. However it is not possible fully to exclude the effect of frame compliance of the Berkovich indenter, and thus C_0 is expected to be an overestimate. Therefore C_{indenter} of a spherical indenter is underestimated

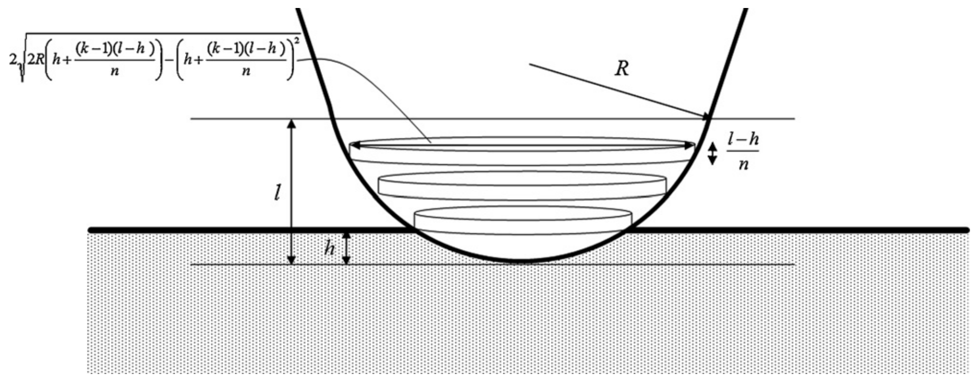

Fig. 3. Infinitesimal deformation and frame compliance in spherical nanoindentation.

and has negative values over 500 nm. From the results in Fig. 2b, the effect of frame compliance of Berkovich on C_0 is not dominant because the relative values and trends are close to the estimated values. Frame compliance directly affects indentation force and depth, which are the fundamental measured data in nanoindentation. Because contact depth and compliance are correlated, we introduced an iteration between them:

$$h^n = h^0 - f(h^{n-1}) \cdot P^0 \tag{10}$$

where h^0 and P^0 are the initial measured indentation depth and force, h^n is the nth calibrated indentation depth, and h^{n-1} is the contact depth calculated from the (n–1)th calibrated indentation depth [4].

Iteration using Eq. (10) and frame compliance function $f(h)$ from Eq. (9) yields a convergent indentation force–depth curve in the fully elastic region. Fig. 4 shows indentation force–depth data as analyzed using constant and indentation–depth-dependent frame compliances. We reevaluated the effective radius using the Hertz equation fitting to indentation force–depth data analyzed by indentation–depth-dependent compliance, and found it to be 4.75 μm. This value is consistent with the nominal radius and that directly measured at large indentation depths by profiling the residual impression as shown in Fig. 1a, suggesting that the large difference in apparent effective radius at small indentation depths probably arises from the use of constant frame compliance. Handling frame compliance as a function of indentation depth is especially important at small indentation depths, as described above.

To verify the real indenter geometry with indentation depths below 90 nm, we directly scanned on the tip using XE-100 AFM (Park Systems, Korea) for a 2 μm × 2 μm area including the tip of the spherical indenter. Fig. 5a shows the top view of scanned area. From the AFM scanning results, we calculated the effective indenter radius. The data points in Fig. 5b indicate the effective radius as evaluated by fitting the radius to profiles ranging to the distance

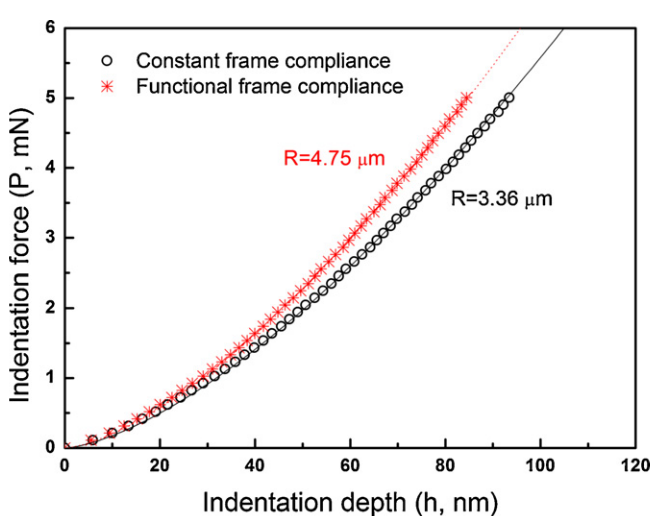

Fig. 4. Indentation force–depth curve as analyzed using and constant frame compliance and indentation–depth-dependent frame compliance and effective radius analyzed by Hertz equation.

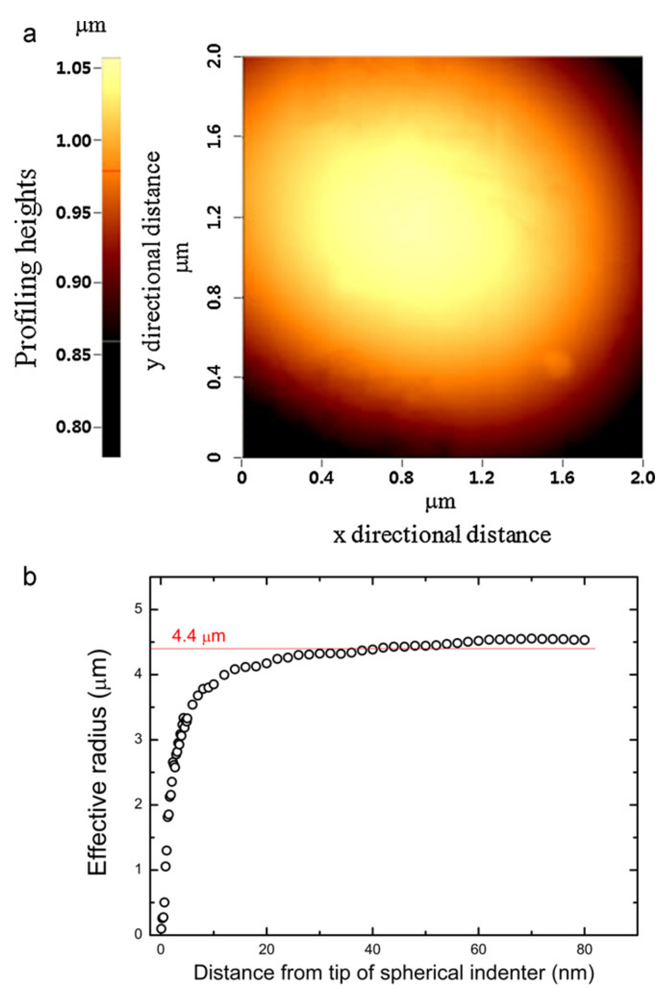

Fig. 5. Direct measurement of spherical indenter geometry with AFM: (a) top-view of scanning image and (b) evaluated effective radii with distance from tip of the spherical indenter.

from the tip of the spherical indenter, from which we could evaluate average effective radius as 4.40 ± 0.11 μm for distances between 10 and 80 nm (except for the initial contact range with distance less than10 nm). This result supports a nominal radius closer to the 4.75 μm evaluated by functional frame compliance method than to the 3.36 μm evaluated by the Hertz method.

4. Conclusions

We investigated calibration issues in real indenter geometry and frame compliance in spherical nanoindentation. We compared two different methodologies; fitting the Hertz equation to force–depth data for indentation depths less than 90 nm and profiling the residual impression for indentation depths greater than 90 nm, which led to a large discrepancy in effective radii. We investigated the variation in frame compliance of the spherical indenter. Calculation of frame compliance for the indenter showed that frame compliance in spherical nanoindentation is not constant but rather a function of indentation depth. The variation in frame compliance was significant at shallow indentation depths because it depends inversely on the logarithmic scale of indentation depth. The functional frame compliance was calculated to obtain real indenter radii using the Hertz equation. We suggest iterative analysis of convergent force–depth data by indentation–depth-dependent frame compliance, since this yields more reasonable indentation force–depth curves. We obtained more consistent indenter radii in the elastic region with the Hertz equation than by profiling residual impression method. We verified the consistent indenter radius evaluated by indentation-depth-dependent frame compliance with direct profiling indenter geometry by AFM.

Acknowledgments

This research was supported by the Converging Research Center Program through the Ministry of Education, Science and Technology (2011K000599). The authors are grateful to Prof. Jae-il Jang of the Division of Materials Science and Engineering, Hanyang University, for valuable discussions and support of the nanoindentation testing.

References

[1] W.C. Oliver, G.M. Pharr, J. Mater. Res. 7 (1992) 564.
[2] ISO/FDIS 14577-1, Metallic materials – instrumented indentation test for hardness and materials parameters. Part 2. Verification and calibration of testing machines (2002).
[3] ASTM E2546-07, Standard Practice for Instrumented Indentation Testing, 2007.
[4] S.K. Kang, J.Y. Kim, I. Kang, D. Kwon, J. Mater. Res. 24 (2009) 2965.
[5] C. Ullner, E. Reimann, H. Kohlhoff, A. Subaric-Leitis, Measurement 43 (2010) 216.
[6] J.H. Ahn, D. Kwon, J. Mater. Res. 16 (2001) 3170.
[7] E.G. Herbert, G.M. Pharr, W.C. Oliver, B.N. Lucas, J.L. Hay, Thin Solid Films 398–399 (2001) 331.
[8] J.Y. Kim, K.W. Lee, J.S. Lee, D. Kwon, Surf. Coat. Technol. 201 (2006) 4278.
[9] K. Ai, L.H. Dai, Scr. Mater. 56 (2007) 761.
[10] S. Pathak, J. Shaffer, S.R. Kalidindi, Scr. Mater. 60 (2009) 439.
[11] W.W. Gerberich, J.C. Nelson, E.T. Lilleodden, P. Anderson, J.T. Wyrobek, Acta Mater. 60 (1996) 3585.
[12] Y.L. Chiu, A.H.W. Ngan, Acta Mater. 50 (2002) 1599.
[13] R.S. Aida, J. Alcala, R.M. Souza, Philos. Magn. 91 (2011) 1370.
[14] H. Bei, E.P. George, J.L. Hay, G.M. Pharr, Phys. Rev. Lett. 95 (2005) 045501.
[15] K.L. Johnson, Contact Mechanics, Cambridge University Press, Cambridge, 1985.
[16] T. Chudoba, M. Griepentrog, A. Dück, D. Schneider, F. Richter, J. Mater. Res. 19 (2004) 301.
[17] M. Herrmann, F. Richter, Philos. Magn. 91 (2011) 1356.
[18] J. Rodríguez, M.A.G. Maneiro, Mech. Mater. 39 (2007) 987.